

The influence of biodiesel fuel on injection characteristics, diesel engine performance, and emission formation



Luka Lešnik^a, Blaž Vajda^a, Zoran Žunič^b, Leopold Škerget^a, Breda Kegl^{a,*}

^aUniversity of Maribor, Faculty of Mechanical Engineering, Smetanova 17, SI-2000 Maribor, Slovenia

^bAVL AST d.o.o., Trg Leona Štuklja 5, SI-2000 Maribor, Slovenia

HIGHLIGHTS

- MCC combustion model is suitable for simulation in M injection system.
- Injection, fuel spray and combustion models give good agreement with experiment.
- Biodiesel properties increase NO_x emission up to 15% relative to diesel.
- Biodiesel properties reduce CO emissions up to 75% relative to diesel.

ARTICLE INFO

Article history:

Received 19 January 2013

Received in revised form 2 May 2013

Accepted 4 May 2013

Keywords:

Heavy-duty diesel engine

Injection system

Biodiesel

Spray development

CO emissions

NO_x emissions

ABSTRACT

The presented work focuses on numerical and experimental analyses of biodiesel fuel's influence on the injection characteristics of a mechanically-controlled injection system, and on the operating conditions of a heavy-duty diesel engine. Addressed are mineral diesel fuel and neat biodiesel fuel made from rapeseed oil. The influence of biodiesel on mechanically controlled injection system characteristics was tested experimentally on an injection system test-bed. The injection test-bed was equipped with a glass injection chamber in order to observe the development of the fuel-spray by using a high-speed camera. The results of the experimental measurements were compared to the numerical results obtained by using our own mathematical simulation program. This program has been used to analyze the influences of different fuel properties on the injection system's characteristics. The photos taken with a high-speed camera were compared to the simulation results obtained by using the AVL FIRE 3D CFD simulation program. This software was used to simulate the fuel-spray development during different stages of the injection process. Furthermore, the influence of biodiesel fuel on the engine operating condition of a heavy-duty diesel engine and its' emission formation was tested experimentally on an engine test-bed, and numerically by using the AVL BOOST software. It was found out that the tested biodiesel could be used as an alternative fuel for heavy-duty diesel engines.

© 2013 Elsevier Ltd. All rights reserved.

1. Introduction

Decreases in fossil-fuel resources and global atmospheric pollution are becoming major problems throughout the World. Biofuels can provide a good alternative to fossil-fuels and they can reduce harmful emissions like carbon monoxide (CO), carbon dioxide (CO₂), unburned hydro carbon (HC) emissions, and soot. In diesel engines, biodiesel can potentially be used instead of mineral diesel fuel. Biodiesel can be made from different raw materials like canola oil, rapeseed oil, animal tallow, algae, and others. The raw material used influence the biodiesel properties that may be more or less similar to the one of mineral diesel. Biodiesel fuels typically consist

of lower alkyl fatty acid, esters of short-chain alcohols, and methanol. Demirbas [1] and Torres et al. [2] investigated the differences in the physical and chemical properties of ethanol–biodiesel fuel-blends and their influence on injection and engine characteristics. The experimentally tested properties were density, viscosity, cold filter plugging, cloud-point, flash-point, and so on. Torres et al. [3] also tested how ethanol addition to mineral diesel fuel influences the operating characteristics of injection systems. Fengkun et al. [4] have tested how different oxygenic fuel additives can contribute to the improvement of diesel and petrol fuel combustion. For this purpose, they experimentally-measured the surface tensions of different diesel and petrol mixtures containing ethanol and other additives. From their results for surface tension, they assessed how the different concentrations of additives influence fuel atomization and combustion. Cecil et al. [5] presented a method for

* Corresponding authors. Tel.: +386 22207732.

E-mail address: breda.kegl@um.si (B. Kegl).

predicting the of biodiesel fuels from their fatty acid compositions. From their results, they assessed how surface tension influences fuel atomization.

Investigations of biodiesel's influence in diesel engines can be divided into three major parts. The influence of biodiesel's fuel properties on the injection system's characteristics, influence on spray formation, and its influence on diesel engine performance and emissions formation [6–16]. Mechanically-controlled and electronically-controlled injection systems have to be considered separately. Kegl and Hribernik [7], and Torres et al. [6], investigated the influence of biodiesel properties on various mechanically-controlled injection systems' operating characteristics, like fueling, mean injection rate, mean injection pressure, injection timing, etc. Thumheer [11] tested different fuel injection strategies in heavy-duty diesel engines equipped with common rail injection systems and their influence on engine performance and emission formation. Hulwan and Joshi [17], and Park et al. [18] also tested how different ethanol, diesel and biodiesel fuel mixtures influence engine operating conditions and emission formation. In [19] an optimization model was developed in order to establish the optimal blend of diesel, ethanol, and biodiesel fuel with the aim to lower the production costs and meet market demands. Kannan et al. [20] investigated how ferric chlorides, used as additives to waste cooking and palm oil based biodiesel, influence the emission formation and engine thermal efficiency. Most researchers agree that the use of biodiesel as a replacement for mineral diesel can contribute to a reduction of HC, CO, CO₂, and soot emissions. The same pattern of emission reduction was also observed with the use of ethanol, diesel, and biodiesel fuel mixtures in [18], where the author also observed a slight decrease in NO_x emissions. Apart from emissions, biodiesel fuels typically cause a reduction in engine power and torque due to their lower calorific values and lead to increased fuel consumption in engines with mechanically controlled injection systems. So far, most investigations are done by using experimental testing combined with numerical simulation. On the other hand, some alternative approaches have also been adopted. For example, Ismail et al. [21] used artificial neural network modeling for nine different engine response parameters. Pandian et al. [22] and Wu and Wu [23] used a response surface method and the Taguchi method, respectively, for the determination of different engine and/or injection system parameters when using biodiesel fuels.

Several different computation fluid dynamic (CFD) simulation programs can be used when simulating diesel spray development. Mostly the Euler–Lagrange approach is adopted, which treats each fuel droplet as an individual particle. Volmajer and Kegl [24] used the FIRE 3D CFD program for simulating the diesel spray by using various injector nozzles. Lucchini et al. [25] used the OpenFOAM simulation software to simulate the fuel spray development. In order to reduce the mesh dependency, they implemented an adaptive mesh refinement technique. Based on experimental results, specific sub-models for spray breakup were developed, tested, and verified. Dynamic (adaptive) mesh refinement technique for

improving spray simulation was also employed by Kolakaluri et al. [26], where it was implemented within the KIVA-4 CFD program. CFD simulation by using the FLUENT software can also be used for analyzing emission formation within the combustion chamber [27], where several different biodiesel were tested and their effect on thermal and prompt NO emissions, and on soot formation was evaluated.

In this paper the influence of biodiesel from rapeseed oil on injection and combustion characteristics of a bus diesel engine with mechanically controlled M injection system is considered at various engine operating regimes. For this purpose, some important engine characteristics were determined by experiment and by numerical simulation. At first, the injection pressure, the needle lift, and the injected fuel per cycle were determined experimentally on a fuel injection system test bed and numerically by using our own mathematical model. Furthermore, to the test bed a glass chamber was added, into which fuel spray was injected in order to record spray development using a high speed camera. Simulations of the spray development were also performed using the AVL FIRE CFD simulation program, and the Euler–Lagrange approach. Finally, the influence of biodiesel on engine torque, power, exhaust gas temperature, NO_x and CO emissions was tested numerically using the AVL BOOST simulation program, and experimentally on the engine test bed under full load, and various engine speeds. The attention is focused on the possibility to replace mineral diesel fuel by pure rapeseed biodiesel in the tested diesel engine.

2. Tested fuels

Mineral diesel fuel D2 that contained no additives and conformed to European standard EN 590, and biodiesel fuel B100 produced from rapeseed oil at Biogoriva, Rače, Slovenia, that conformed to European standard EN 14214, were used during the presented study. It is well-known that fuel properties have a noticeable influence on injection and engine characteristics. For that reason, some of the more important properties of mineral diesel and biodiesel fuel were measured experimentally by using different test methods that correspond to European or other standards. Fuel density was measured at 15 °C by using a method that conformed to European standard EN ISO 12185, kinematic viscosity was measured at 40 °C by using a test method that conformed to European standard EN ISO 3104, and fuel composition was measured by using the test method ASTM D 5291. The sound velocity in fuels was measured at different pressures up to 700 bar and is presented in Fig. 1. Measures were based on the monitoring of pressure wave propagation along a specified length in a high pressure tube with two piezoelectric pressure transducers that were located at the opposite sides of high pressure tube. A small pump with a plunger was used to induce system pressure and pressure waves that were monitored using piezoelectric transducers. Some of the used fuel properties are presented in Fig. 1 and Table 1.

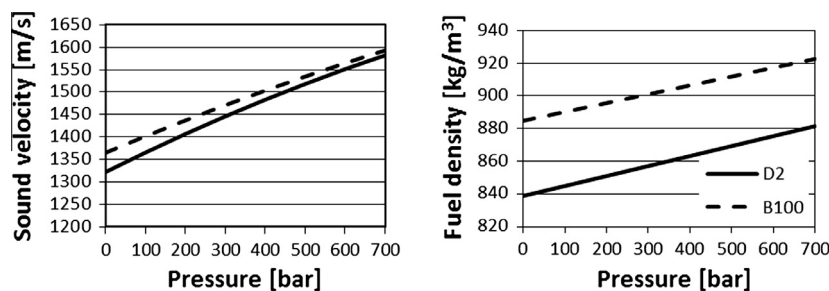


Fig. 1. Fuel properties.

Table 1
Fuel properties.

Fuel	D2	B100
Density at 15 °C (kg/m ³)	838.8	884.8
Kinematic viscosity at 30 °C (mm ² /s)	3.34	5.51
Surface tension at 30 °C (N/m)	0.0255	0.028
Calorific value (MJ/kg)	42.8	38.2
Cetane number	45	51
Stoichiometric air–fuel ratio	14.7	13
Oxygen mass fraction	0	0.1039
Hydrogen mass fraction	13.87	11.07
Carbon mass fraction	86.13	76.68
Ester content (%(m/m))	–	97.3
Total glycerol (%(m/m))	–	0.176
Monoglycerides content (%(m/m))	–	0.59
Diglycerides content (%(m/m))	–	0.14
Triglycerides content (%(m/m))	–	0.05
Flash point (°C)	66	138.5
Water content (mg/kg)	50	150
Sulfur content, WD-XRF (mg/kg)	31	5.8

3. Experimental measures

Experimental measures of the fuel injection system were performed on a Friedmann–Maier type 12 H 100-h test-bed. The tested injection system was a mechanically-controlled injection system from 6 cylinders MAN diesel engine, as schematically presented in Fig. 2. The fuel injection system consisted of a BOSCH PE-S6A95D410LS2542 high pressure pump, high pressure tubes and BOSCH DLLA 5S834 injectors with one nozzle hole. Some of fuel injection system properties are presented in Table 2. In order to measure the most important injection parameters, the test bed and injection system were fully instrumented with measuring equipment. At both sides of the high pressure tube of the first

injector, two pressure transducers were mounted in order to measure the injection pressure in the high pressure tube. A specially designed inductance sensor was developed to measure the needle lift. An optic sensor was used to determine the top dead-center (TDC) position and the camshaft angle. The injected fuel quantity per cycle was measured by collecting the injected amount of fuel over 500 cycles in glass gauges. The pump load was determined by rack positioning, which means that under a single operating regime the usages of different fuels caused the fueling to be slightly different. The injection characteristics were tested using mineral diesel and biodiesel fuels under full load, and three different pump speeds, 500, 800, and 1100 rpm.

A glass chamber was added to the injector test bed for the purpose of monitoring fuel spray development. The fuel from the first injector was injected into the glass chamber under atmospheric pressure and monitored using a high speed camera. This high speed camera was connected to a computer that was further connected to and synchronized with the injector test bed to ensure the exact time (camshaft angle) at which each photo was taken by the high speed camera. Based on a signal from the injector test bed, a trigger signal from the personal computer was sent to the high speed camera for starting the picture capturing. The process of spray development monitoring is schematically presented in Fig. 3. The high speed camera recorded 2500 frames per second at a resolution of 128 × 512 pixels. The start of photographing was triggered based on a signal from the injector test bed. Three consecutive injections were monitored for every speed of pump rotation. The length of the fuel spray jet was determined by processing the image pixels by a specially developed LabVIEW program.

A heavy-duty 6 cylinders MAN D2566 MUM four stroke bus diesel engines was used for the experimental measures of the

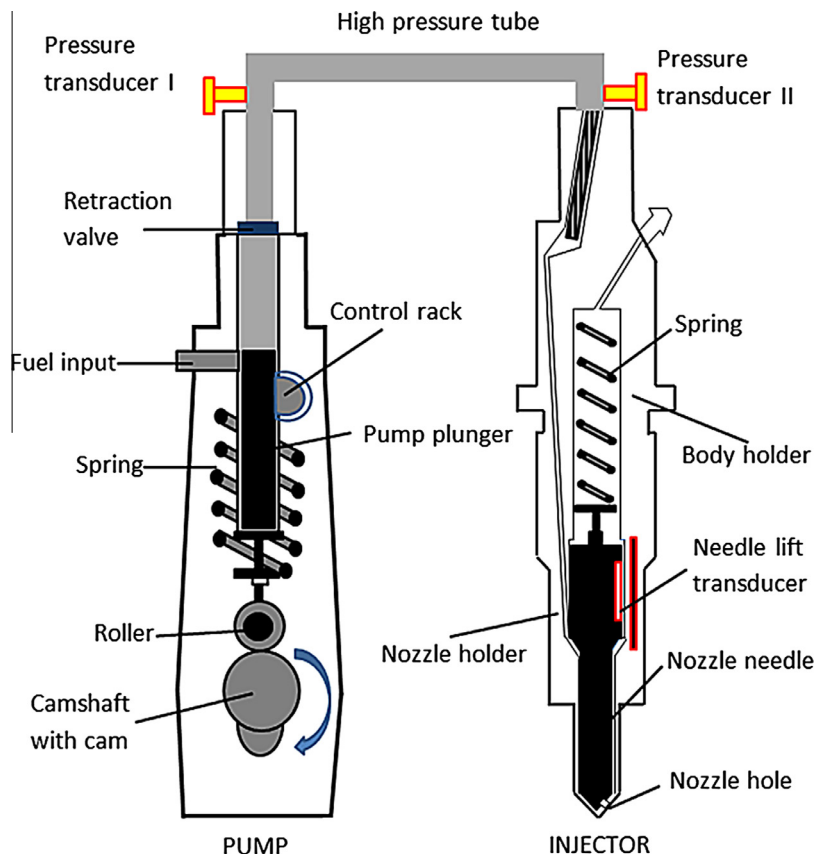


Fig. 2. Scheme of injection system [7].

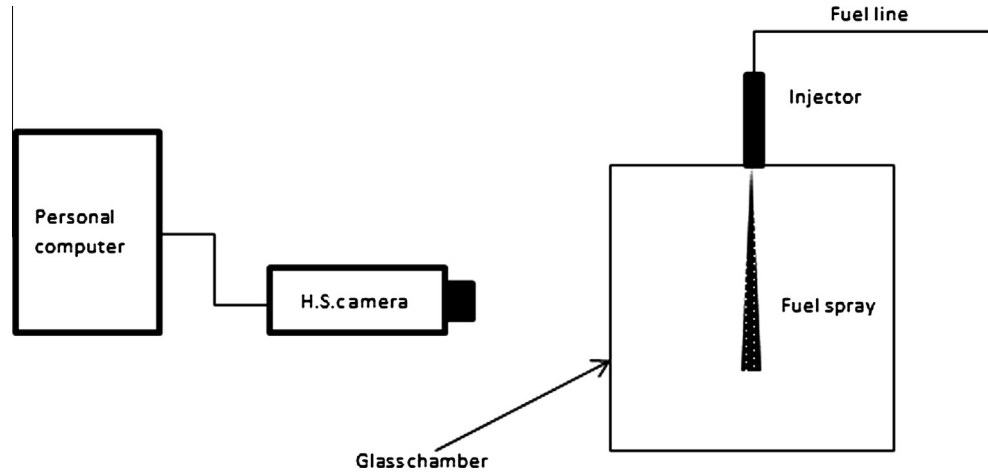


Fig. 3. Scheme of spray development monitoring.

Table 2
Fuel injection system specification.

Fuel injection pump type	Bosh PES 6A 95D 410 LS 2542
Pump plunger (diameter × lift)	9.5 mm × 8 mm
Fuel tube (length × diameter)	1024 mm × 1.8 mm
Injection nozzle (number × nozzle hole diameter)	1 × 0.68 mm
Maximal needle lift	0.3 mm

Table 3
Engine specifications.

Item	Specification
Engine	MAN D2566 MUM four stroke
Gas exchange	Natural aspirated
Number of cylinders	6
Bore (mm)	125
Stroke (mm)	155
Total displacement (ccm)	11413
Compression ratio	17.5
Injection type	Direct injection
Fuel pump	BOSCH PES6A95D410LS2542
Injector	BOSCH DLLA 5S834
Injection pump timing (° BTDC)	23
Needle opening pressure (bar)	175
Maximum injection pressure (bar)	650

biodiesel influence on the engine characteristics. Some of the diesel engine specifications are presented in Table 3. A piezoelectric pressure transducer was mounted in the combustion chamber of the first engine cylinder, and was used for measuring the in-cylinder pressure. A fuel flow meter was used for measuring the engine's hourly fuel consumption, while an air flow meter was used at the engine's air intake for measuring the engine's air consumption. Several thermocouples were used for monitoring the air intake, exhaust gas, and the engine oil temperature.

All measuring equipment from the engine and injector test bed was connected to a multifunctional data acquisition card, and a personal computer for monitoring and storing all the measured values. The LabVIEW software was used for to build the application that stored all measured values automatically.

4. Fuel injection system simulations

The BKIN mathematical model was used for numerical simulation of the injection process. In BKIN the processes in the high-

pressure pump, high-pressure tube, and fuel injector are simulated by using a one-dimensional model, consisting of 11 ordinary differential equations [31]. The fuel properties of mineral diesel and biodiesel fuels were implemented into the simulation program in order to obtain a good agreement between the experimental and numerical results. The fuel properties implemented in the simulation program were sound velocity, density of the liquid and vapor phase, bulk modulus, and surface tension.

5. Spray simulation

Spray simulations were performed using the AVL FIRE computational fluid dynamic (CFD) program. In the numerical simulation, fuel was injected into the cylinder through the injector nozzle, placed on the top of the cylinder. An unstructured grid with refined elements in the center of the cylinder, where the injector nozzle is placed, was used. The grid structure is presented in Fig. 4, while some specific grid and cylinder parameters are presented in Table 4.

Euler–Lagrange (E–L) multiphase simulation approach was adopted in this study. This approach is commonly used when simulating highly dispersed flows where the volume fraction of the dispersed phase is relatively small. The spray simulations are based on a statistical method also called the discrete droplet method (DDM). This method introduces droplet parcels within the flow domain with the initial conditions of position, size, temperature, velocity, and number of particles in each parcel. Full two-way interaction between the continuous gas phase and dispersed liquid phase is taken into account during simulations. For the continuous phase the mass and momentum conservation laws can be written as

$$\frac{\partial \alpha_c \cdot \rho_c}{\partial t} + \nabla \alpha_c \cdot \rho_c \cdot v = \sum_{d=1}^N m_{cd} \quad (1)$$

$$\frac{\partial \rho_m \cdot v}{\partial t} + \nabla \rho_m \cdot v^2 = -\alpha_m \cdot \nabla p + \nabla (\tau + T^t) + \rho_m \cdot g + \sum_{d=1}^N M_{cd} + v \cdot \sum_{d=1}^N m_{cd} \quad (2)$$

where α_c is the volume fraction of the continuous phase, ρ_c represent the density, v the velocities of all the phases involved in the flow, \sum_{cd}^m and \sum_{cd}^M represent the interfacial mass and momentum exchanges between the continuous phase c and the dispersal phase d , m represents the homogeneous mixture, p is the pressure and g is

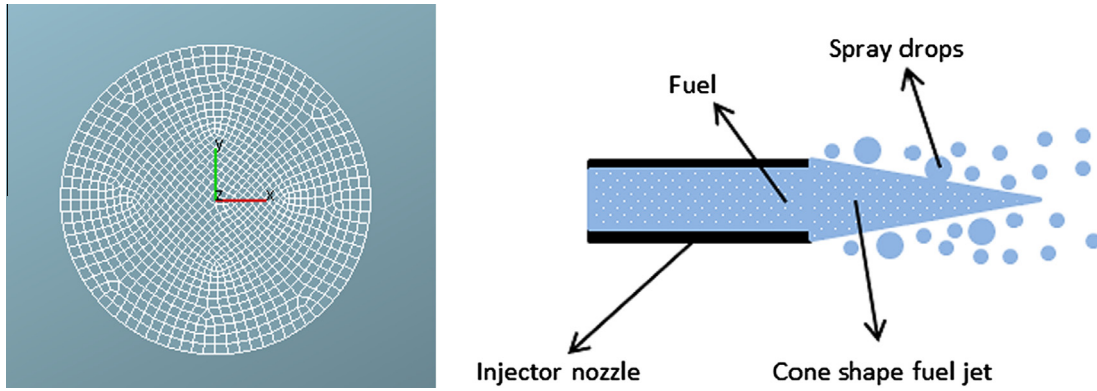


Fig. 4. Grid cross section and core injection primary breakup model.

Table 4
Grid parameters.

Number of grid elements	167620
Cylinder length (m)	0.4
Cylinder diameter (m)	0.07

the gravity vector. T^t is the Reynolds stress tensor and τ the shear stress tensor.

The following ordinary differential equations can be written for every particle of the disperse phase, traveling along the path x_p , the sum of all forces $\sum F$ acting on the particle, and the heat transfer \dot{Q} on the particle surface A_p .

$$\frac{dx_p}{dt} = v_p \quad (3)$$

$$m_p \cdot \frac{dv_p}{dt} = \sum F \quad (4)$$

$$\dot{Q} = \alpha \cdot A_p \cdot (T_a - T_f) \quad (5)$$

where v_p is the velocity of the particle, and m_p is its mass.

Nozzle flow induced turbulence and aerodynamic interaction between the fuel and surrounding air have a significant influence on fluid spray break-up and droplet formation. Primary break-up models are used to describe the fuel droplet sizes and speed close to the nozzle orifice. A core injection primary break-up model was used in the presented study. It assumes that the fuel spray at the nozzle exit is cone shaped and the individual droplets are separated from it gradually, Fig. 4.

$$\frac{dR}{dt} = \frac{L_A}{\tau_A} \quad (6)$$

$$L_A = C_2 \cdot C_\mu \frac{k^{1.5}}{\varepsilon} \quad (7)$$

$$D_d = L_A \quad (8)$$

$$\tau_A = C_1 \cdot \tau_T + C_3 \cdot \tau_W \quad (9)$$

$$v_{drop} = \frac{L_A}{\tau_A} \quad (10)$$

The characteristic turbulent length L_A is calculated from the turbulent kinetic energy k and the change of the initial bubble diameter R . The initial droplet diameter D_d is equal to the characteristic turbulent length. The initial droplet velocity v_{drop} can be calculated from the ratio between characteristic turbulent length and turbulent kinetic energy. The characteristic break-up time τ_A is a function of characteristic turbulent break-up time τ_T and characteristic aerodynamic break-up time τ_W . C_1 , C_2 and C_3 are model coefficients and C_μ is the nozzle exit coefficient.

The influences of different fuel properties on aerodynamic break-up time can be explained by using the Kelvin–Helmholtz instability model (K–H). The K–H model assumes that instabilities (waves) formed on the spray surface are driven by lift force, the force of surface tension, and the force caused by the Bernoulli effect. The lift force is proportional to the difference in fluid densities, $\Delta\rho = \rho_1 - \rho_2$, and to the wave number κ . It can either stabilize or destabilize any instability formed by aerodynamic interactions, depending on the fluid density. The surface tension force is always stabilizing and is stronger in liquids where the surface tension S is higher. The force of the Bernoulli effect is always destabilizing and is driven by the difference in fluid velocities Δv which create pressure differences on the interface surface between the fuel and surrounding air. The effect of K–H instability is schematically presented in Fig. 5 and by the following equation:

$$\frac{g \cdot \Delta\rho}{\kappa} + S \cdot \kappa - \frac{\rho_1 \cdot \rho_2 (\Delta v)^2}{\rho_1 - \rho_2} < 0 \quad (11)$$

A secondary break-up model is needed for simulating spray formation and droplet break-up far from the injector nozzle orifice. The spray break-up mechanism is very complex and is a combination of induced turbulence, cavitation, bubble-collapse, aerodynamic forces, and used fuel characteristics. The standard wave secondary break-up model was used. The corresponding equations can be written as

$$\frac{dr}{dt} = \frac{-(r - r_{stable})}{\tau_a} \quad (12)$$

$$\tau_a = \frac{3.726 \cdot C_2 \cdot r}{\Lambda \Omega} \quad (13)$$

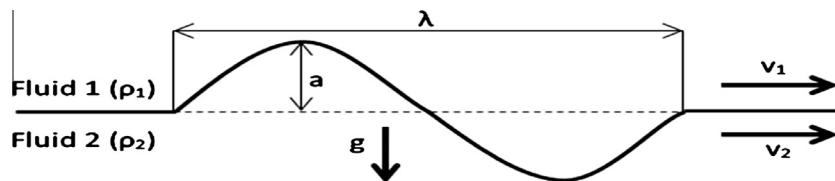


Fig. 5. K–H instability.

$$r_{stable} = C_1 \cdot \Lambda \tag{14}$$

$$\Lambda = 9,02r \frac{(1 + 0.45 \cdot Oh^{0.5})(1 + 0.4 \cdot T^{0.7})}{(1 + 0.87 \cdot We_g^{1.67})^{0.6}} \tag{15}$$

$$\Omega = \left(\frac{\rho_g r^3}{\sigma}\right)^{-0.5} \cdot \frac{0.34 + 0.38 \cdot We_g^{1.5}}{(1 + Oh) \cdot (1 + 1.4 \cdot T^{0.6})} \tag{16}$$

Here, any change in the droplet radius r is a function of the droplet break-up time τ_a , which is a function of the wave length Λ formed on the droplet surface and wave growth rate Ω . The wave length and wave growth rates are functions of the Ohnesorge number Oh and the Weber number We . The $k - \epsilon$ turbulent model was used during all simulations.

6. Engine simulation

Numerical simulations of mineral diesel and biodiesel combustion processes and the analysis of biodiesel on heavy duty diesel engine characteristics were done by using the AVL BOOST software. The Chmela and Orthaber MCC combustion model [28] was used, which enables the determination of NO_x and CO emissions. A virtual model of tested MAN engine is shown on Fig. 6.

6.1. Combustion model

The heat released during the fuel combustion in the combustion chamber is the only source of energy in internal combustion en-

gines. The MCC combustion model divides combustion into two stages. The first stage is premixed (kinetic) combustion dQ_{PMC} that occurs after the ignition delay interval ends. The second part of the combustion is the mixing controlled (diffusion) combustion dQ_{MCC} that follows the premixed part of the combustion and begins when all the fuel/air mixture from the first part of the combustion has burned.

$$\frac{dQ_c}{d\alpha} = \frac{dQ_{total}}{d\alpha} = \frac{dQ_{MCC}}{d\alpha} + \frac{dQ_{PMC}}{d\alpha} \tag{17}$$

In the premixed part of combustion the fuel that was vaporized and mixed with fresh air during the ignition delay interval is burned. Because of the large amount of excess air at this stage, the fuel/air mixture burns rapidly. In this work the Vibe function was used to calculate the heat released $\frac{dQ_{PMC}}{d\alpha}$ during the premixed combustion, as given by Eqs. (18)–(21):

$$\frac{dQ_{PMC}}{d\alpha} = \frac{a}{\Delta\alpha_c} (m + 1) \cdot y^m \cdot e^{-a \cdot y^{(m+1)}} \tag{18}$$

$$Q_{PMC} = m_{f, id} \cdot C_{PMC} \tag{19}$$

$$\Delta\alpha_c = \tau_{id} \cdot C_{PMC-Dur} \tag{20}$$

$$y = \frac{\alpha - \alpha_{id}}{\Delta\alpha_c} \tag{21}$$

The shape parameter m was set to 2 for this purpose and the Vibe parameter to 6.9. The duration of ignition delay τ_{id} and the crankshaft angle α_{id} at which the ignition delay ended (start of

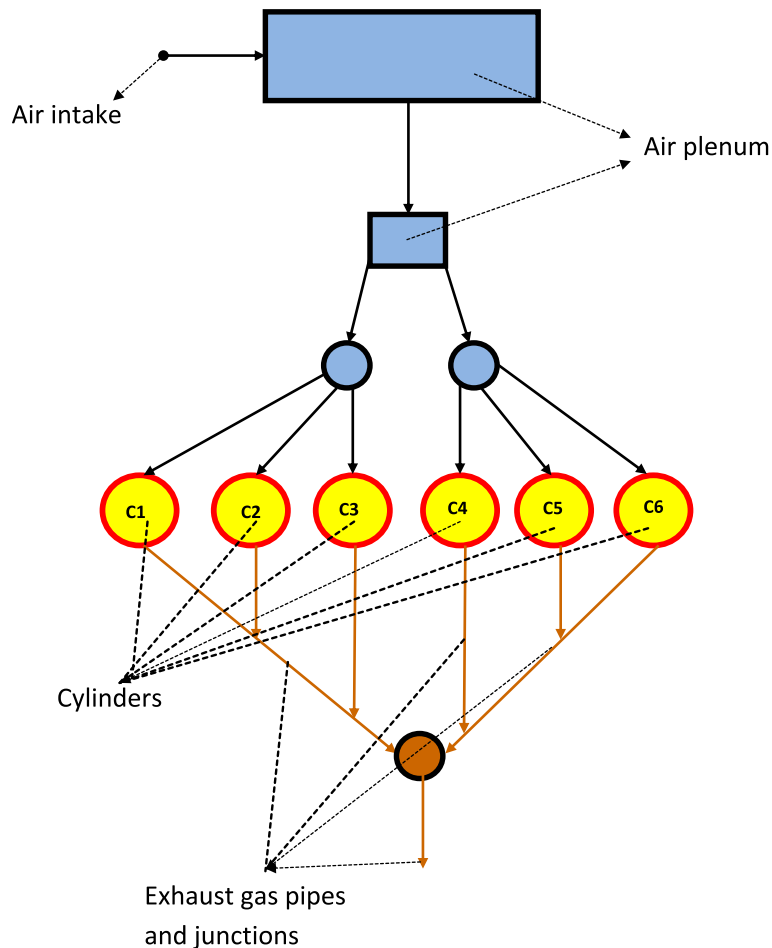


Fig. 6. Virtual model of engine.

the combustion), were calculated using the ignition delay model, developed by Andree and Pachernegg, Eq. (22). In Eq. (22) I_{id} represents the ignition delay interval, T_{UB} the temperature of unburned zone, and T_{ref} the reference temperature, which was set to 505 K. The ignition delay duration τ_{id} is the difference between the crankshaft angle α_{SOI} at start of injection and the crankshaft angle α_{id} at which the ignition delay ended and combustion started.

$$\frac{dI_{id}}{d\alpha} = \frac{1}{C_{IDCF}} \cdot \frac{T_{UB} - T_{ref}}{Q_{ref}} \quad (22)$$

$$\tau_{id} = \alpha_{id} - \alpha_{SOI} \quad (23)$$

During the mixing controlled part of the combustion, the fuel that was injected after the ignition had start, is burned. The model assumes that the amount of heat dQ_{MCC} released during this stage of combustion is a function of the fuel available for combustion f_1 (m_f, Q_{MCC}) and the local density $f_2(k, V_c)$ of turbulent kinetic energy in the cylinder,

$$\frac{dQ_{MCC}}{d\alpha} = C_{comb} f_1(m_f, Q_{MCC}) f_2(k, V_c) \quad (24)$$

The amount of fuel that was available for combustion was calculated as a function of the injected fuel m_f and the amount of burned fuel $\frac{Q_{MCC}}{LCV}$ as

$$f_1(m_f, Q_{MCC}) = \left(m_f - \frac{Q_{MCC}}{LCV} \right) (w_{O_2,available})^{C_{EGR}} \quad (25)$$

C_{EGR} is the EGR parameter related to the available oxygen $w_{O_2,available}$, if the engine is equipped with an EGR system.

The local density of the turbulent kinetic energy k is a function of the mixing rate constant C_{Rate} and the cylinder volume V_c and can be calculated by using Eqs. (27) and (28).

$$f_2(k, V_c) = C_{Rate} \cdot \frac{\sqrt{k}}{\sqrt[3]{V_c}} \quad (26)$$

$$k = \frac{E_{kin}}{m_{f,inj} \cdot (1 + \lambda_{diff} \cdot m_{stoich})} \quad (27)$$

$$\frac{dE_{kin}}{dt} = 0.5 \cdot C_{turb} \cdot \dot{m}_f \left(\frac{\dot{m}_f}{\rho_f \mu A} \right)^2 - C_{diss} \cdot E_{kin}^{1.5} \quad (28)$$

where E_{kin} represents the kinetic jet energy, λ_{diff} is the air excess ratio for diffusion burning, m_{stoich} is the stoichiometric mass of fresh charge, $m_{f,inj}$ is the actual mass of injected fuel, ρ_f is fuel density and μA is the effective nozzle hole area. C_{turb} and C_{diss} are turbulence and dissipation parameters of the combustion model, respectively.

The values of the model parameters were set within the prescribed limit intervals, as suggested by the developers of AVL BOOST.

6.2. Emission formation models

The emission model for the computation of NO_x formation, used during the presented study, was based on the Pattas and Häfner NO_x formation model [29]. The rate of NO_x formation was computed by using the following equation:

$$r_{NO} = C_{PM} \cdot C_{KM} \cdot 2 \cdot (1 - \alpha_{NO}) \cdot \frac{r_{1,NO}}{1 + \alpha_{NO} R_2} \cdot \frac{r_{4,NO}}{1 + R_4} \quad (29)$$

where C_{PM} and C_{KM} present the post processing and kinetic multi-player, α_{NO} is the ratio between the actual and computed NO molar concentrations, R_2 and R_4 are the ratios of the reaction rates $r_{i,NO}$, $i = 1, \dots, 6$, obtained by Eqs. (33)–(38)

$$\alpha_{NO} = \frac{C_{NO,act}}{C_{PP} \cdot C_{NO,cal}} \quad (30)$$

$$R_2 = \frac{r_1}{r_2 + r_3} \quad (31)$$

$$R_4 = \frac{r_4}{r_5 + r_6} \quad (32)$$

$$r_{1,NO} = k_1 \cdot C_{N_2} \cdot C_O \quad (33)$$

$$r_{2,NO} = k_2 \cdot C_{O_2} \cdot C_N \quad (34)$$

$$r_{3,NO} = k_3 \cdot C_{OH} \cdot C_N \quad (35)$$

$$r_{4,NO} = k_4 \cdot C_{N_2O} \cdot C_O \quad (36)$$

$$r_{5,NO} = k_5 \cdot C_{O_2} \cdot C_{N_2} \quad (37)$$

$$r_{6,NO} = k_6 \cdot C_{OH} \cdot C_{N_2} \quad (38)$$

where the coefficients k_i , $i = 1, \dots, 6$ are obtained as

$$k_i = k_{0,i} \cdot T^a \cdot e^{\left(\frac{-T_{Ai}}{T}\right)}, \quad i = 1 \dots 6 \quad (39)$$

The computation of the reaction rates is based on the Zeldovich mechanism. The symbols c_i denote the molar concentrations under equilibrium conditions, expressed in mole/cm³, $k_{0,i}$, a and T_{Ai} are the reaction rate computation constants, and T is the temperature.

The CO emission formation model used is based on the Onorati CO formation model [30] which computes the final rates of the CO products as

$$r_{CO} = C_{Cons} \cdot (r_{1,CO} + r_{2,CO})(1 + \alpha_{CO}) \quad (40)$$

In Eq. (40) α_{CO} represents the ratio between the actual and computed CO molar concentrations, obtained by Eq. (41). The symbols $r_{1,CO}$ and $r_{2,CO}$ are the reaction rates obtained by Eqs. (42) and (43), where T represents the temperature

$$\alpha_{CO} = \frac{C_{CO,act}}{C_{CO,cal}} \quad (41)$$

$$r_{1,CO} = 6.76 \cdot 10^{10} \cdot e^{\left(\frac{T}{1102}\right)} \cdot C_{CO} \cdot C_{OH} \quad (42)$$

$$r_{2,CO} = 2.51 \cdot 10^{12} \cdot e^{\left(\frac{-24055}{T}\right)} \cdot C_{CO} \cdot C_{O_2} \quad (43)$$

The final rates for NO_x and CO were computed by using Eqs. (29) and (40), and expressed as concentrations in mole/cm³s.

7. Results

The influence of biodiesel on injection characteristics of a mechanically-controlled injection system was analyzed experimentally and numerically. All the testing was performed at full load and at three various pump speeds (500, 800, and 1100 rpm). The experimental testing was performed on an injection system test bed whilst numerical simulations were made by using the BKIN simulation software.

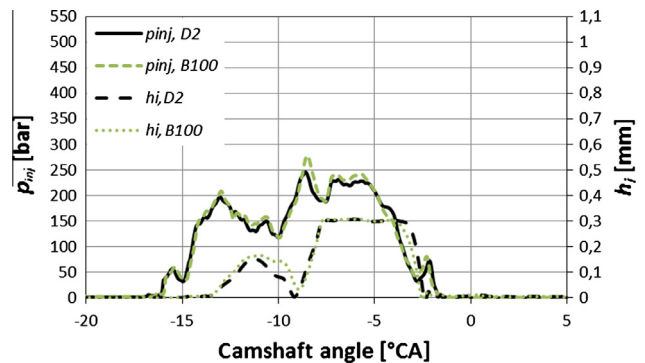


Fig. 7. Experimental results at full load and 500 rpm of pump speed.

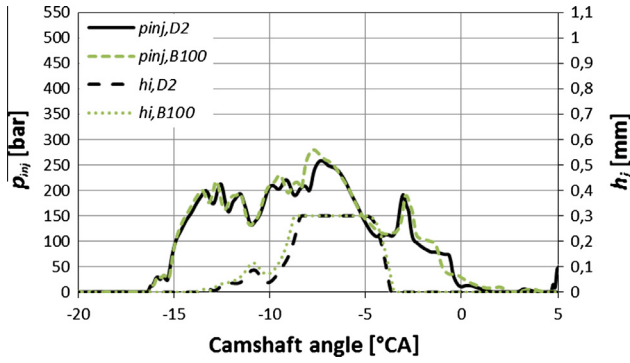


Fig. 8. Numerical results at full load and 500 rpm of pump speed.

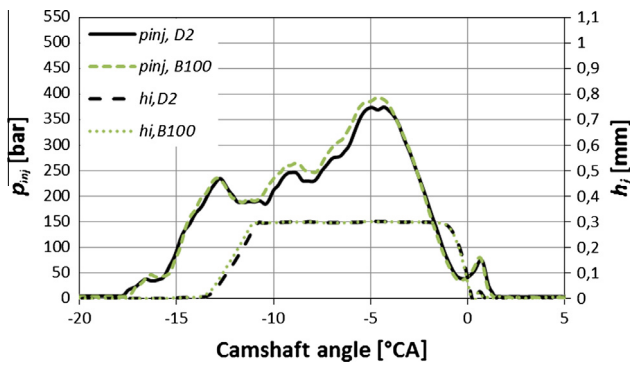


Fig. 9. Experimental results at full load and 800 rpm of pump speed.

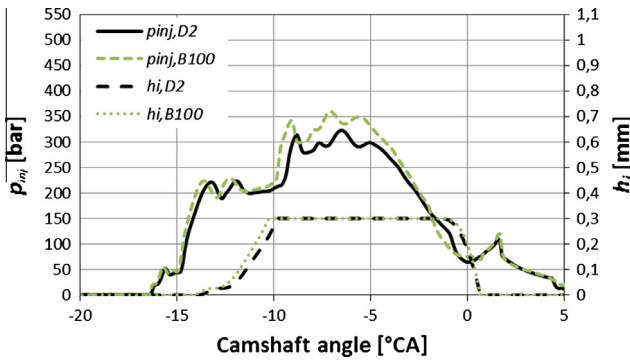


Fig. 10. Numerical results at full load and 800 rpm of pump speed.

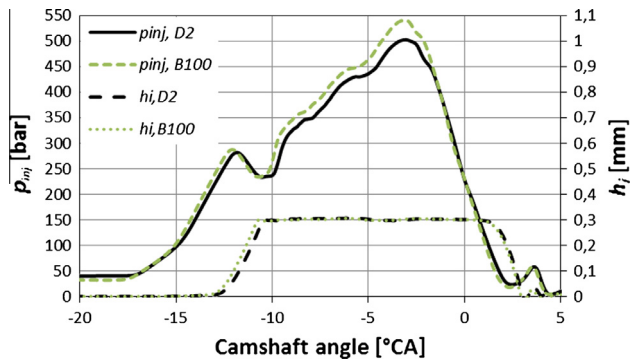


Fig. 11. Experimental results at full load and 1100 rpm of pump speed.

The experimental and numerical results of the needle lift h_i and injection pressure p_{inj} (measured and computed at the end of the high pressure tube) for the diesel (D2) and biodiesel (B100) fuels are presented in Figs. 7–12.

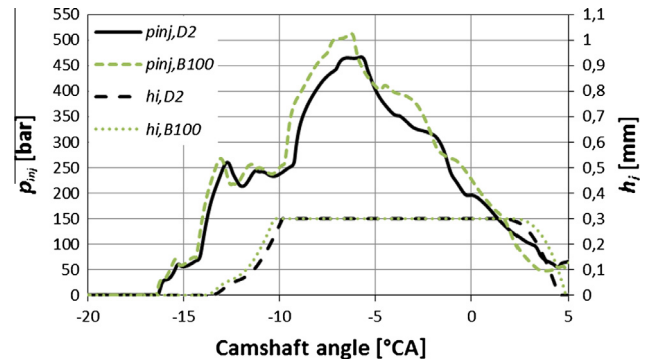


Fig. 12. Numerical results at full load and 1100 rpm of pump speed.

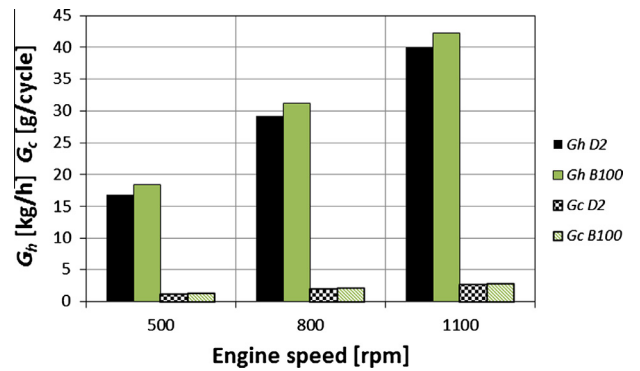


Fig. 13. Fuel consumption G_n and injected mass of fuel per cycle G_c .

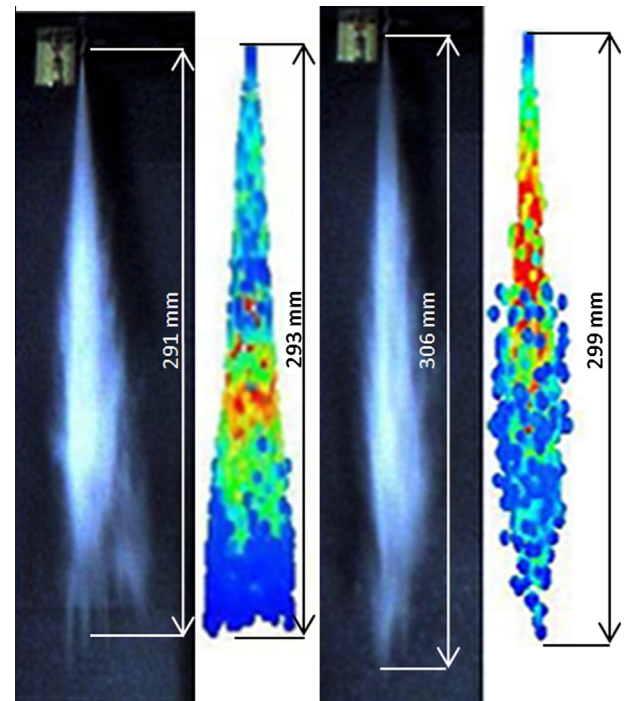


Fig. 14. Experimental and numerical results of spray jet at 500 rpm pump speed for diesel (left) and biodiesel (right).

It can be seen from Figs. 7–12 that the variation in fuel properties, caused by replacing mineral diesel by biodiesel, influences the start of the needle lift and injection timing. The higher density and sound velocity of biodiesel result in advanced needle opening and advanced injection timing at all tested operating regimes. This was obtained experimentally and numerically. The advanced start of injection caused an increase in the in-cylinder pressure which resulted in an increase of NO_x emissions.

The variation in fuel properties also influences the injection duration, which is longer when using biodiesel. The longer injection durations result in a larger amount of injected fuel mass per cycle G_c , which increases the hourly fuel consumption G_h , as presented in Fig. 13.

The experimental and numerical results also indicate that biodiesel usage results in a faster increase of the injection pressure p_{inj} . By using biodiesel, the maximum values of injection pressure as well as the mean injection pressure are higher than those obtained by mineral diesel. Higher mean injection pressure may lead to longer spray jet. Besides of this, fuel density, kinematic viscosity, and surface tension, which are higher for biodiesel, could also influence the fuel spray development. Experimental and numerical results, illustrated in Figs. 14–16 show the influence of fuel properties on the spray length and shape. The experimentally obtained sprays were filmed by using a high speed camera which records 2500 frames per second. The spray lengths from the photos were determined from the image pixel size and the ratio of the picture

size to spray length. The numerical simulations of the spray were done by using the AVL FIRE CFD software. The lengths of all sprays are summarized in Table 5.

The comparisons of experimentally and numerically obtained spray jets, presented on Figs. 14–16, show that biodiesel typically produces longer spray tip penetration lengths and narrower spray angles. Partially, this is the consequence of higher biodiesel spray velocities. Furthermore, the higher surface tension of biodiesel also reduces the aerodynamic influence on the spray break-up, which also contributes to longer spray tip penetration. This can be explained by the Kelvin–Helmholtz instability model, where the higher surface tension of biodiesel results in a higher surface tension force. The higher surface tension force leads to smaller surface-instabilities (waves), which also contributes to smaller influence of the Bernoulli effect force. All these effects result in longer and narrower sprays.

The longer and narrower sprays of biodiesel may lead to poorer droplet formation and larger Sauter mean diameters D_{32} . This could result in poorer evaporation of the biodiesel fuel, which could, in combination with the higher flash point of biodiesel, increase the ignition delay.

It can be seen from Table 5 that the biodiesel spray jets are approximately 2–6% longer than the diesel sprays. The numerical and experimental results agree quite well. Only at 1100 rpm pump speed, the numerical results show a somewhat larger deviation, approximately 12%, from the experimental results.

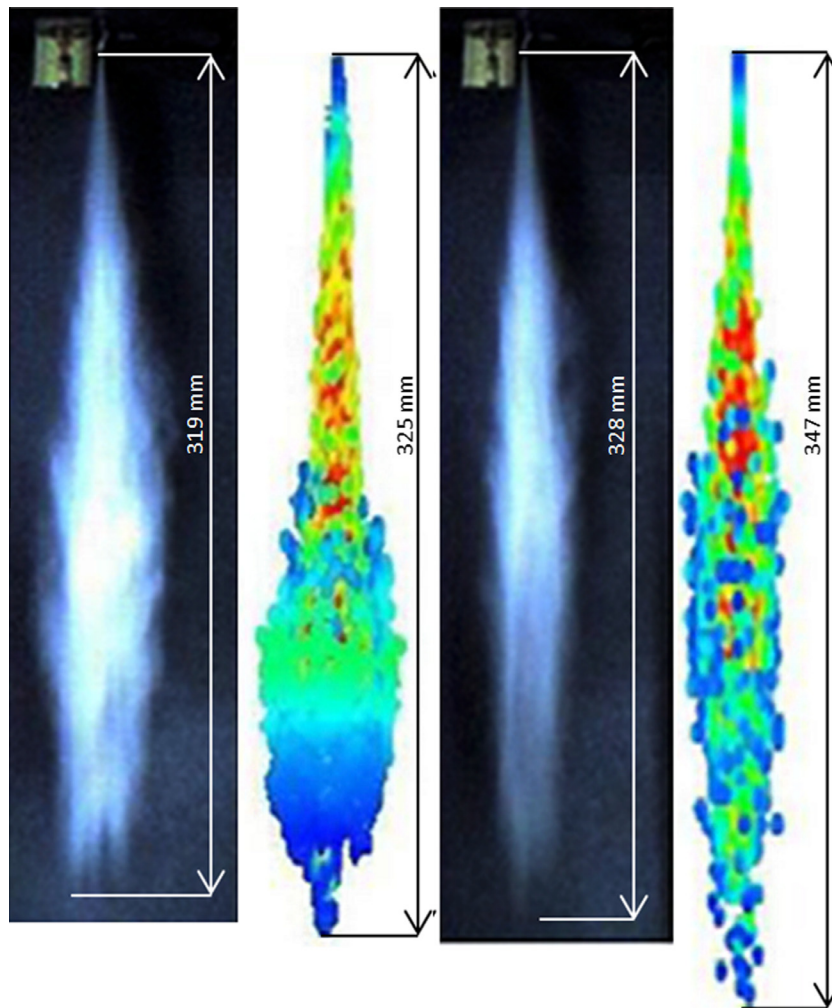


Fig. 15. Experimental and numerical results of spray jet at 800 rpm pump speed for diesel (left) and biodiesel (right).

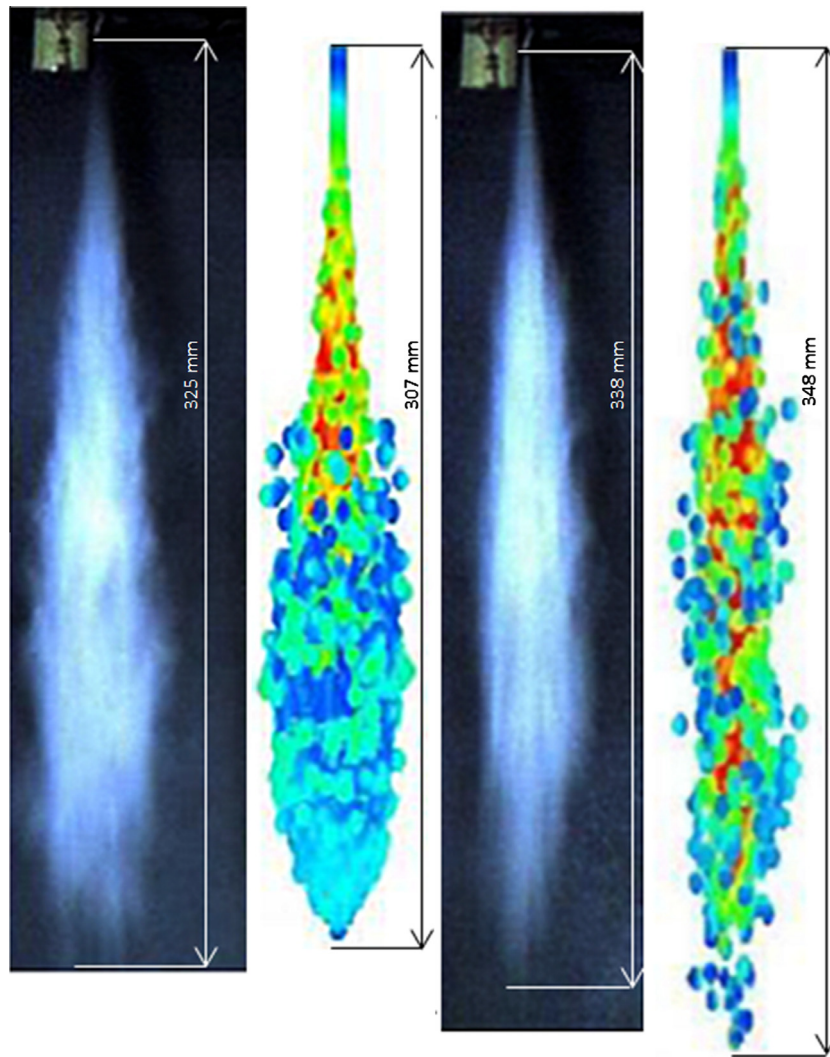


Fig. 16. Experimental and numerical results of spray jet at 1100 rpm pump speed for diesel (left) and biodiesel (right).

Table 5
Experimental and numerical obtained spray lengths.

	500 rpm	800 rpm	1100 rpm
D2 Exp.	291 mm	319 mm	325 mm
B100 Exp.	306 mm	328 mm	338 mm
D2 Ns.	293 mm	325 mm	307 mm
B100 Ns.	299 mm	347 mm	348 mm

The biodiesels influence on the engine performance and emissions formation in the tested bus diesel engine are presented in Figs. 17–20. Fig. 17 shows the experimental and numerical results for mineral diesel, while Fig. 18 shows the same results for biodiesel. It can be seen that the agreement between numerical results and experiment is mostly quite well. The most evident differences, about 12%, were obtained for engine torque. All other differences are in range 5–10%. In general, the experimental and numerical re-

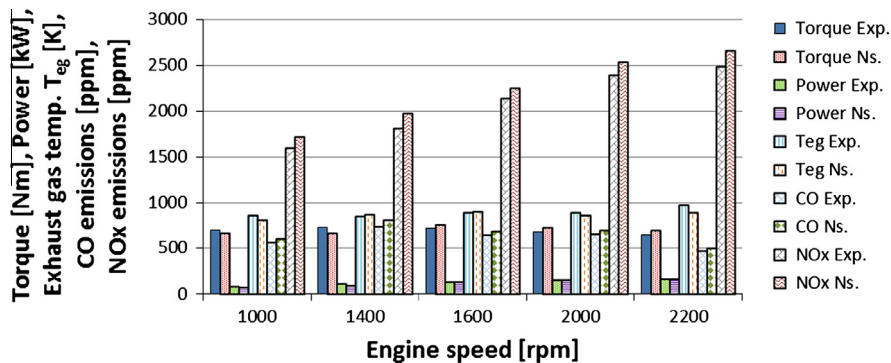


Fig. 17. Comparison of experimental (Exp.) and numerical (Ns.) results for diesel fuel.

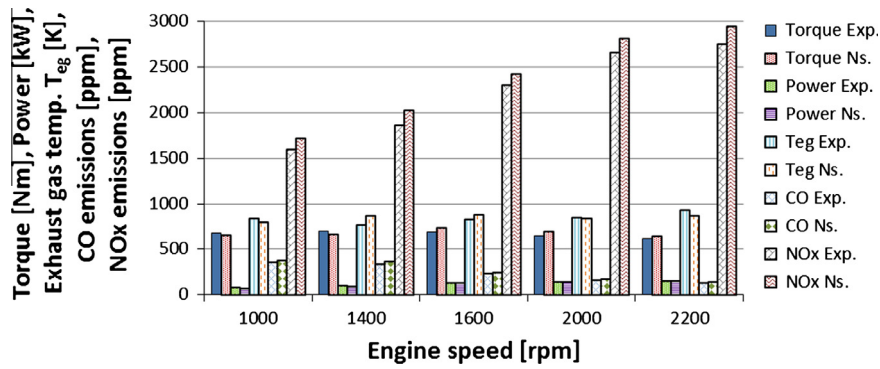


Fig. 18. Comparison of experimental (Exp.) and numerical (Ns.) results for biodiesel fuel.

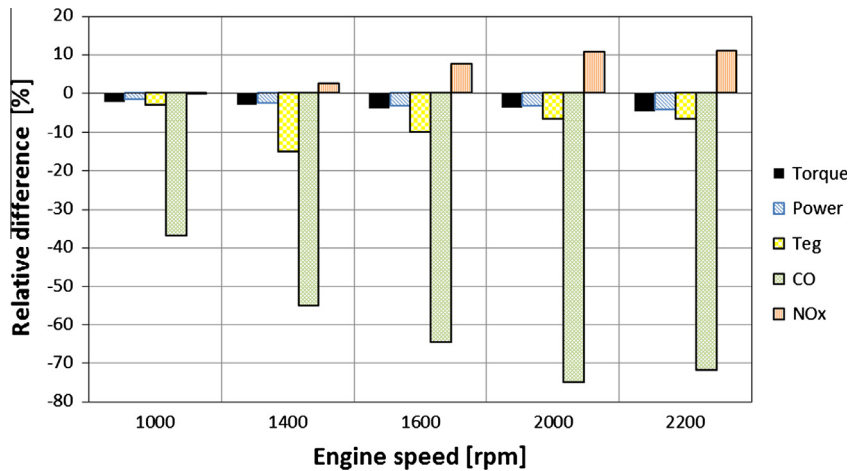


Fig. 19. Experimental results of biodiesel influence on diesel engine performance.

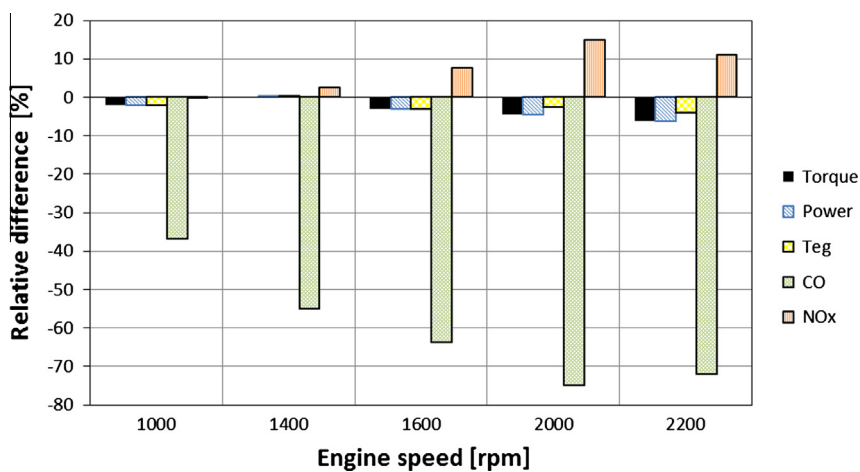


Fig. 20. Numerical results of biodiesel influence on diesel engine performance.

sults agreed well and showed the same trends for mineral diesel and biodiesel fuel usage.

Figs. 19 and 20 show the relative differences (in percent) of the investigated quantities, obtained by using mineral diesel and biodiesel. The relative differences, for example for engine torque M , were calculated as $\left(1 - \frac{M_{B100}}{M_{D2}}\right) \cdot 100\%$. All the numerical simulations and experimental measures were made at full load and at various engine speeds.

Figs. 17–20 show the influence of biodiesel on the engine power, torque, exhaust gas temperature, and on CO and NO_x emissions. The lower calorific value of biodiesel contributes to lower engine power and torque. From both, the experimentally and numerically obtained results, it can be seen that the decrease of engine power and torque was higher when increasing the engine speed. The maximum decrease of power and torque is 5% by experiment and 8% by numerical simulation, both being obtained at maximum engine power at 2200 rpm.

The lower calorific value of biodiesel results also in a reduction of the engine exhaust gas temperature. The maximum decrease of the exhaust gas temperature was observed by experiment at peak torque condition (1400 rpm). Numerical simulation showed a smaller decrease. The reason for this is probably in the insufficient description of heat losses in the exhaust pipes in the numerical simulation.

By using biodiesel, the emissions of CO have been reduced at all operating conditions. The higher content of oxygen in biodiesel contributes to better oxidation processes in the combustion chamber and reduces the production of CO emission. On the other hand more oxygen also promotes the production of nitric oxides NO_x . Furthermore, the advanced injection timing, caused by biodiesel usage, leads to higher in-cylinder pressure and consequently to higher NO_x production.

8. Conclusions

The influence of pure biodiesel usage on injection, fuel spray, and engine characteristics was investigated experimentally and numerically for a bus MAN diesel engine with mechanically controlled M injection system. The injection characteristics were determined experimentally on an injection system test bed and numerically by using the BKIN mathematical model. The fuel spray was determined numerically by using the Euler–Lagrange multiphase simulation approach of AVL FIRE CFD software and experimentally by spray injection into a glass chamber under atmospheric pressure. The engine characteristics were determined experimentally on an engine test bed and numerically by using the AVL BOOST software and the mixed controlled combustion model. All the measurements and simulations were made under full load and at various engine speeds. Based on the obtained results, the following conclusions can be made:

- Higher sound velocity and a bulk modulus of biodiesel fuel lead to advanced needle lift and injection timing in mechanically controlled injection systems.
- Advanced injection timing increases the in-cylinder pressure.
- The advanced start of needle lift results in longer injection duration, which raises (compared to mineral diesel) the amount of injected biodiesel per cycle.
- The differences in the fuel properties between tested biodiesel and diesel result in a higher maximum and higher mean value of the injection pressure in mechanically controlled injection systems.
- Higher mean injection pressure results in longer spray penetration lengths of biodiesel. Other biodiesel properties like higher density, sound velocity, and a higher bulk modulus also contribute to longer penetration lengths of the biodiesel spray jets.
- The influences of different fuel properties on the spray penetration lengths can be explained by the Kelvin–Helmholtz instability model.
- Longer and narrower sprays of biodiesel fuel increase the Sauter mean diameter of biodiesel droplets. Combined with higher flash-point and poorer evaporation of biodiesel, this increases the ignition delay.
- Lower calorific value of biodiesel reduced the power and torque of the tested engine. All numerical and experimental results indicate that the maximum reductions of engine power and torque are most exposed at higher engine speeds. The maximum reduction of engine power and torque is about 5% which is less than the difference in the calorific value of biodiesel (approximately 10%).
- Lower calorific value of the tested biodiesel also results in lower exhaust gas temperature. A significant exhaust gas temperature reduction was observed during the experimental measure-

ments. Numerical simulation showed a smaller reduction. This is probably caused by insufficient description of heat losses in the exhaust pipes.

- Oxygen content in biodiesel contributes to better oxidation processes within the combustion chamber. This reduces CO emission and promotes higher NO_x emission. The advanced start of injection, caused by biodiesel usage, also contributes to a higher production of NO_x emissions.
- The numerically obtained results agreed relatively well with the experimental results. This indicates that, to some extent, numerical simulations may be used as a replacement for expensive experimental measurements.

At the bottom line, it looks like the tested biodiesel could be used as replacement for mineral diesel in heavy duty diesel engines that are similar to the tested engine.

Acknowledgements

This work was supported by the Slovenian Research Agency (ARRS). We also wish to thank AVL LIST GmbH for their support by providing the AVL-AST software program used during the research.

References

- [1] Demirbas A. Progress and recent trends in biodiesel fuels. *Energy Convers Manage* 2009;50:14–34.
- [2] Torres Jiménez E, Svoljšak M, Gregorc A, Lisec I, Pilar Dorado M, Kegl B. Physical and chemical properties of ethanol–biodiesel blends for diesel engines. *Energy Fuels* 2010;24(3):2002–9.
- [3] Torres Jiménez E, Svoljšak M, Gregorc A, Lisec I, Pilar Dorado M, Kegl B. Physical and chemical properties of ethanol–diesel fuel blends. *Fuel* 2011;90(2):795–802.
- [4] Fengkun W, Jiangato W, Zhigang L. Surface tension of mixture of diesel oil or gasoline and dimethoxymethane, dimethyl carbonate or ethanol. *Energy Fuels* 2006;20:2471–4.
- [5] Cecil AWA, Watts KC, Ackman RG. Prediction of the surface tension of biodiesel fuels from their fatty acid composition. *JAOCS* 1999;76:317–23.
- [6] Torres Jiménez E, Kegl M, Dorado R, Kegl B. Numerical injection characteristics analysis of various renewable fuel blends. *Fuel* 2012;97:832–42.
- [7] Kegl B, Hribernik A. Experimental analysis of injection characteristics using biodiesel fuel. *Energy Fuels* 2006;20:2239–48.
- [8] Kegl B. Influence of biodiesel on engine combustion and emission characteristics. *Appl Energy* 2011;88:1803–12.
- [9] Hribernik A, Kegl B. Influence of biodiesel fuel on the combustion and emission formation in a direct injection (DI) Diesel engine. *Energy Fuels* 2007;21:1760–7.
- [10] Roy MM, Wang W, Bujold J. Biodiesel production and comparison of emissions of a DI diesel engine fueled by biodiesel–diesel and canola oil–diesel blends at high idling operations. *Appl Energy* 2013;106:198–208.
- [11] Hribernik A. The influence of biodiesel fuel on the injection, combustion, emissions and performance of a direct-injection diesel engine. *J Mech Eng* 2006;52(1):3–14.
- [12] Thumheer T, Edenhauser D, Soltic P, Schreiber D, Kirchen P, Sankowski A. Experimental investigation on different injection strategies in a heavy-duty diesel engine: emissions and loss analysis. *Energy Convers Manage* 2011;52:457–67.
- [13] Macor A, Avella F, Faedo D. Effect of 30% v/v biodiesel/diesel fuel blends on regulated and unregulated pollutant emissions from diesel engines. *Appl Energy* 2011;88:4989–5001.
- [14] Yamane K, Ueta A, Shimamoto Y. Influence of physical and chemical properties of biodiesel fuel on injection, combustion and exhaust emission characteristics in a DI–CI engine. The fifth international symposium on diagnostics and modeling of combustion in internal COMBUSTION engines (COMODIA) 2001;402:409.
- [15] Öner C, Altun S. Biodiesel production from inedible animal tallow and an experimental investigation of its use as alternative fuel in a direct injection diesel engine. *Appl Energy* 2009;86:2114–30.
- [16] Lapuerta M, Rodriguez-Fernandez J, Agudelo JR. Diesel particulate emissions from used cooking oil biodiesel. *Bioresour Technol* 2008;99:731–40.
- [17] Holwan DB, Joshi SV. Performance, emission and combustion characteristic of a multicylinder DI diesel engine running on diesel–ethanol–biodiesel blends of high ethanol content. *Appl Energy* 2011;88:5042–55.
- [18] Park SH, Cha J, Lee CS. Impact of biodiesel in bioethanol blended diesel on the engine performance and emissions characteristics in compression ignition engine. *Appl Energy* 2012;99:334–43.

- [19] Lin J, Gaustad G, Trabold TA. Profit and policy implications of producing biodiesel–ethanol–diesel fuel blends to specification. *Appl Energy* 2013;104:936–44.
- [20] Kannan GR, Karvembu R, Anand R. Effect of metal based additive on performance, emission and combustion characteristics of diesel engine fuelled with biodiesel. *Appl Energy* 2011;88:3694–703.
- [21] Ismail HM, Ng HK, Queck CW, Gan S. Artificial neural network modeling of engine-out responses for a light-duty diesel engine fuelled with biodiesel blends. *Appl Energy* 2012;92:769–77.
- [22] Pandian M, Sivapirakasam SP, Udayakumar K. Investigation on the effect of injection system parameters on performance and emission characteristics of a twin cylinder compression ignition direct injection engine fuelled with pongamia biodiesel–diesel blend using response surface methodology. *Appl Energy* 2011;88:2663–76.
- [23] Wu HW, Wu ZY. Using Taguchi method on combustion performance of a diesel engine with diesel/biodiesel blend and port-inducting H₂. *Appl Energy* 2013;104:362–70.
- [24] Volmajer M, Kegl B. Diesel-spray analysis. *J Mech Eng* 2001;47:627–36.
- [25] Lucchini T, D'Errico D, Ettorre D. Numerical investigation of the spray-mesh-turbulence interactions for high-pressure, evaporating sprays at engine conditions. *Int J Heat Fluid Flow* 2011;32:285–97.
- [26] Kolakaluri R, Li Y, Kong SC. A unified spray model for engine spray simulation using dynamic mesh refinement. *Int J Multiph Flow* 2010;36:858–69.
- [27] Ng HK, Gan S, Ng JH, Pang KM. Simulation of biodiesel combustion in a light-duty diesel engine using integrated compact biodiesel–diesel reaction mechanism. *Appl Energy* 2013;102:1275–87.
- [28] Chmela F, Orthaber G. Rate of heat release prediction for direct injection diesel engines based on purely mixing controlled combustion. SAE Technical Paper 1999-01-0186.
- [29] Pattas K, Häfner G. Stickoxidbildung bei der ottomotorischen Verbrennung. *MTZ* 1973;12:397–404.
- [30] Onorati A, Ferrari G, D'Errico G. 1D unsteady flows with chemical reactions in the exhaust duct-system of S.I. engines: predictions and experiments. SAE Technical Paper 2001-01-0939.
- [31] Kegl B. An improved mathematical model of conventional FIE processes. SAE Technical Paper 1995-950079.